FIELDS OF STORED ENERGY ASSOCIATED WITH LOCALIZED NECKING OF STEEL

ANDRÉ CHRYSOCHOOS, BERTRAND WATTRISSE,
JEAN-MICHEL MURACCIOLE AND YVES EL KAÏM

LMGC, UMR 5508 Université Montpellier 2 - CNRS

This paper describes an experimental procedure for the simultaneous determination of heat sources and mechanical energy involved locally during a heterogeneous tensile test. This procedure involves two complementary imaging techniques: digital image correlation (DIC) and infrared thermography (IRT). The first technique gives displacement fields from which strains are derived while the second provides temperature fields with which the heat sources are estimated using a local form of the heat equation. Moreover, a method based on integration of equilibrium equations under the plane stress assumption is used to determine the stress distribution during the test. The distribution of the local deformation energy developed by the material is then assessed using stress and strain-rate fields.

Tensile tests were performed on thin flat steel samples. The results revealed early and gradual development of strain localization within the gauge part of the specimen. Energy balances were performed inside and outside the necking zone based on the assumption that the thermoelastic part of the behaviour remains linear and isotropic. Finally, indirect estimate of the stored energy led us to compute the time course of the local Taylor–Quinney coefficient.

Keywords: digitial image correlation, infrared thermography, dissipation, stored energy, plasticity, localization.

Introduction

The conversion of mechanical energy into heat has been investigated in a wide range of materials by many researchers, including [Taylor and Quinney 1934; Schmidt et al. 1945; Chrysochoos and Martin 1989; Rittel 1999]. Using different experimental arrangements (calorimeter [Shenogin et al. 2002], thermocouples [Zehnder et al. 1998], IR sensors [Guduru et al. 2001; Chrysochoos and Louche 2000]), these studies gave similar results, showing that a variable amount of mechanical energy is converted into heat during inelastic transformation. Such techniques generally provide a macroscopic estimate of the Taylor–Quinney coefficient that links mechanical and dissipated energies. Here *macroscopic* means at the scale of the sample gauge part. This coefficient plays a key role in the modelling of plasticity each time the dissipated energy has to be introduced within a pure mechanical elastic-plastic framework. It has been used to compute the plastic strain-induced heat without having to invoke a particular thermodynamic framework [Batra and Chen 2001; Campagne et al. 2005; Rusinek et al. 2007]. Moreover, we stress that this coefficient is nearly always regarded as a constant material parameter, independent of the loading path and strain hardening history. In such particular cases, the stored energy ratio is then equal to the ratio of the stored energy rate, as we will see hereafter. This latter ratio often appears in the heat equation associated with anisothermal viscoplastic models developed to describe dynamic localization mechanisms [Mercier and Molinari 1998; Rosakis et al. 2000]. Nevertheless, in the case of heterogeneous

loading (necking, shear bands, etc.), energy fields are then both representative of the material behaviour combined with structure effects. Under such conditions, the overall Taylor–Quinney coefficient can no longer be only representative of the material behaviour.

In this paper, we present a specific setup for local estimate of different terms of the energy balance for quasistatic, heterogeneous tests. This setup combines two imaging techniques, that is, digital image correlation (DIC) and infrared thermography (IRT). The experimental design enables us to estimate the local distribution of deformation energy rate developed by the material and heat sources induced by the loading. DIC techniques are now commonly used to measure displacement and strain fields on the surface of thin specimens [Chu et al. 1985]. Besides, IRT camera performances have been considerably improved with the advent of infrared focal plane array sensors (IRFPA). These new cameras provide IR films with fine spatial resolution, low thermal noise, and reasonably high frame rates for quasistatic mechanical tests.

In what follows, we first review the theoretical background used to define the energy balance. We then describe the different devices involved in the setup and experimental procedure. In the third part, we detail the data processing procedures and their validation. Finally, we present and discuss some results obtained during straining of an interstitial-free steel (commercial grade: IF–Ti).

Energy balance and heat equation

To draw up the energy balance, we worked within the classical formalism of generalised standard materials [Halphen and Nguyen 1975] which are sometimes used to deal with material behaviours [Lemaitre and Chaboche 1985], particularly in plasticity [Lubliner 1991]. In this framework, the thermodynamic state of each volume element of the material is characterised by a finite set of variables. In the case of plasticity, this set includes the absolute temperature T, a strain tensor denoted by ϵ, and a vector α whose components characterize the microstructural state of the material. The chosen thermodynamic potential associated with such a state variable set is the Helmholtz free energy $\psi(T, \varepsilon, \alpha)$.

The dissipation is a volume heat source associated with irreversible processes induced by deformation mechanisms and heat diffusion. Its definition is classically derived from the local expression of the 2nd principle of thermodynamics defining the irreversible entropy source. As usual, we suppose that the intrinsic (mechanical) dissipation d_1 and the thermal dissipation d_2 are separately positive. With the chosen set of state variables, d_1 is defined by

$$d_1 = \sigma : D - \rho \frac{\partial \psi}{\partial \varepsilon} : \dot{\varepsilon} - \rho \frac{\partial \psi}{\partial \alpha} \cdot \dot{\alpha} \geq 0, \tag{1}$$

where ρ is the mass density, σ is the Cauchy stress tensor, and D the Eulerian strain-rate tensor. The superimposed dot represents the time derivative. Naturally, the equality $d_1 = 0$ corresponds to mechanically reversible processes. Note that the intrinsic dissipation d_1 is the difference between the deformation energy rate $w^{\bullet}_{\text{def}}$, and the sum of the elastic $w^{\bullet}_{\text{e}}$ and stored $w^{\bullet}_{\text{s}}$ energy rates

$$w^{\bullet}_{\text{def}} = \sigma : D, \tag{2}$$

$$w^{\bullet}_{\text{e}} + w^{\bullet}_{\text{s}} = \rho \frac{\partial \psi}{\partial \varepsilon} : \dot{\varepsilon} + \rho \frac{\partial \psi}{\partial \alpha} \cdot \dot{\alpha}, \tag{3}$$

In Equations (2) and (3), the notation $()^\bullet$ means that the variation of () is path-dependent. These different energies are therefore not state functions *a priori*. We define the corresponding energy variations by

$$w_x = \int_{t_0}^{t} w_x^\bullet \, d\tau,$$

where x symbolizes the energy type (for example, deformation, elastic, stored) while t_0 and t are respectively the times of initial and current states. Similarly, the dissipated energy variation is defined by

$$w_\mathrm{d} = \int_{t_0}^{t} d_1 \, d\tau.$$

Temperature variations within the sample are governed by the heat equation. Combining the first and second principles of thermodynamics, we derive its following local expression

$$\rho C \dot{T} + \mathrm{divq} = \mathrm{d_1} + \mathrm{r_e} + \mathrm{w}_\mathrm{tec}^\bullet + \mathrm{w}_\mathrm{tmc}^\bullet, \tag{4}$$

where C stands for the specific heat capacity at constant ϵ and α, while q is the heat influx vector. Assuming a Fourier's law of heat conduction ($q = -k \ \mathrm{grad}\, T$, where k is the constant isotropic conduction coefficient), the left hand side of Equation (4) becomes a partial derivative operator applied to the temperature field T.

Heat sources responsible for temperature variations within the specimen are gathered on the right hand member of Equation (4). They correspond to the intrinsic dissipation d_1, the external volume heat supply r_e, and thermomechanical couplings $w_{tec}^\bullet$ and $w_{tmc}^\bullet$. The term $w_\mathrm{tec}^\bullet$ represents the famous thermoelastic coupling (that is, Lord Kelvin's term), and $w_\mathrm{tmc}^\bullet$ represents all other possible thermomechanical couplings associated with interactions between the temperature and microstructure. In the general case, the sum $w_\mathrm{tec}^\bullet + w_\mathrm{tmc}^\bullet$ reads

$$w_\mathrm{tec}^\bullet + w_\mathrm{tmc}^\bullet = \rho T \frac{\partial^2 \psi}{\partial T \, \partial \varepsilon} : \dot{\varepsilon} + \rho T \frac{\partial^2 \psi}{\partial T \, \partial \alpha} \cdot \dot{\alpha}.$$

In the following, we will assume that the thermoelastic part of the behaviour remains linear and isotropic. We will also neglect all other thermomechanical couplings. This latter hypothesis is justified by the fact that temperature variations remain relatively small, thus inducing no microstructure variation (no self-induced annealing). We thus introduce $w_\mathrm{h}^\bullet$ as the overall heat source defined by $w_\mathrm{h}^\bullet = d_1 + w_\mathrm{tec}^\bullet$ and verifying

$$\rho C \dot{\theta} - k \, \Delta\theta = w_\mathrm{h}^\bullet + r_\mathrm{e} \tag{5}$$

with θ being the local temperature difference $T - T_0$, where T_0 is the current room temperature.

In this setting, the stored energy ratio can then be defined by

$$F_w = \frac{w_\mathrm{s}}{w_{\mathrm{i}n}} = \frac{w_\mathrm{def} - w_\mathrm{e} - w_\mathrm{d}}{w_\mathrm{def} - w_\mathrm{e}} = \frac{w_\mathrm{s}}{w_\mathrm{s} + w_\mathrm{d}}.$$

The difference $w_\mathrm{def} - w_\mathrm{e}$ represents the inelastic work w_in. In the case of plastic hardening at finite strain, the elastic energy generally remains very low relative to the deformation energy so that $F_w \approx 1 - w_\mathrm{d}/w_\mathrm{def}$.

As often supposed in the literature, the stored energy ratio is considered as a constant regardless of the initial hardening state and the loading path (typically $F_w = 0.1$). In this particular case, the ratio of the stored energy rate is also constant and equal to the stored energy ratio itself

$$\dot{F}_w = \frac{d}{dt}\left(\frac{w_s}{w_{in}}\right) = \frac{w_{in} w_s^{\bullet} - w_{in}^{\bullet} w_s}{w_{in}^2} = 0 \Rightarrow F_{w^{\bullet}} = \frac{w_s^{\bullet}}{w_{in}^{\bullet}} = F_w. \tag{6}$$

Conversely, if the stored energy ratio changes, it is no longer equal to the stored energy rate ratio.

Experimental procedure

The experimental tests involved performing, at room temperature, displacement-controlled tensile loading at constant velocity ($v_0 = 250\,\mu\mathrm{m\,s^{-1}}$). The following constant dimensions were allocated to the gauge part of the specimen: the gauge length L_0 and depth D_0 were 50 and 0.3 mm, respectively. Conversely, the width $W_0(X)$ might depend on the longitudinal Lagrangian coordinate X to force, for example, the development of the strain localization around a given cross-section. We chose $W_0 = 12.5$ mm for samples with constant W_0. The depth was set at a particularly low measurement to ensure the plane stress hypothesis and legitimate the hypothesis of uniform strain in the depth direction. A simultaneous record of infrared and visible images was performed on each side of the sample surface $L \times W$ during tensile straining. Figure 1 illustrates the experimental set-up designed for this purpose. It involves a MTS hydraulic testing machine (frame: 100 kN, load cell: 25 kN), a Cedip Jade III infrared camera and a Camelia 8M high resolution CCD camera. The optical axis of both cameras was set perpendicularly to the frame of the testing machine, and it remained fixed during the test.

The main characteristics of the two cameras are given in Table 1. The chemical composition of the material tested is given in Table 2.

Each camera was controlled by a separate computer. A specific electronic device was designed to synchronise the frame grabbing of the two cameras. The principle of this device is as follows. A frequency generator is used to produce the trigger signal of the master camera. This frequency is divided or multiplied by an integer factor to generate the trigger signal of the slave camera. Each time an image acquisition is completed, the analogical signals provided by the machine sensors are digitised, and the

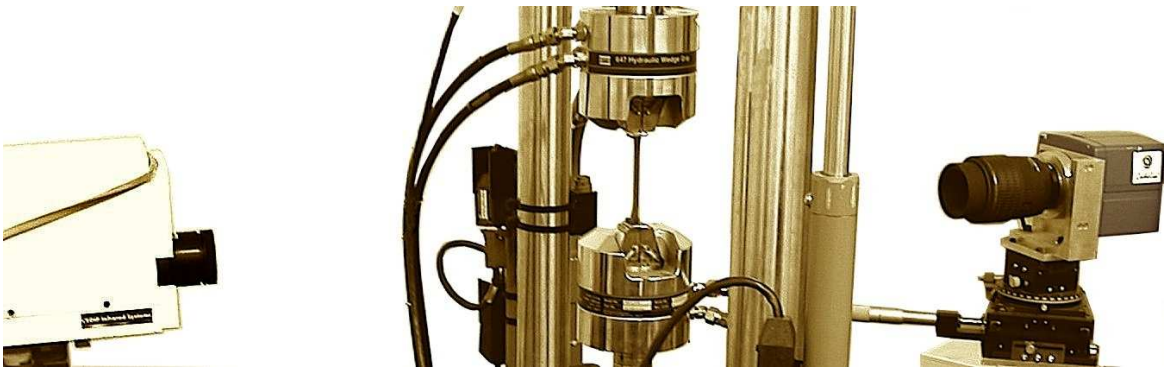

Figure 1. Experimental set-up.

	image size (pix)	scale factor (μm pix^{-1})	frame rate (Hz)
IR: Cedip Jade III	320×240	524	25
CCD: Camelia 8M (binning: 4×4)	875×575	136	5

Table 1. Main camera characteristics.

time is given, on each acquisition computer, by a common clock having a 0.1 ms period. Using this device, we estimated that the synchronisation error between the two cameras was less than 0.05 ms.

Data processing

This section briefly reviews the numerical processing principles developed to determine the different energy fields. We focus particularly on the validation procedure improvements to check the data processing.

Visible images. The surface of the specimen observed by the visible CCD camera is speckled with white paint in order to obtain a random pattern defining the local optical signature of each material surface element (MSE). A classical digital image correlation algorithm allowed us to determine the in-plane components of the displacement field on a regular rectangular grid. The in-plane velocity and strain components were derived from the displacement data by a numerical differentiation method based on a local polynomial approximation of the displacement field [Wattrisse et al. 2001a]. The local time fitting of displacement fields involves a 2nd order polynomial while the local space fitting is associated with a coupled 1st order polynomial of the two in-plane coordinates. The choice of the approximation zone AZ is very important in the differentiation process. The optimized AZ depends on the signal-to-noise ratio and the amplitude of the sought derivatives. The image processing remains then relevant as long as the localization zone is greater than AZ. The camera resolution led us to choose centred AZ spanning around ± 2.5 s by ± 3.5 mm by ± 3.5 mm. In such conditions, the incertitude on strain measurements was estimated at 5×10^{-4} [Wattrisse et al. 2001a].

Using the kinematical data obtained by the DIC algorithm, we constructed the local stress distribution, assuming a quasistatic, plane stress, isochoric transformation. For each acquisition time t, corresponding to an applied load $F(t)$, the tensile component of the stress tensor σ_{xx} was assumed to be homogeneously distributed over each cross-section $S(X,t) = W(X,t) \times D(X,t)$ of the specimen

$$\sigma_{xx}(X,t) = \frac{F(t)}{S_0(X) \cdot \exp(-\varepsilon_{xx}(X,t))} \tag{7}$$

	C	Mn	P	S	Si	Al	N	Ti
% (w)	0.003	0.15	0.007	0.007	0.007	0.02	0.003	0.06

Table 2. Chemical composition of the tested steel [Béranger et al. 1994].

where ϵ henceforth represents the Hencky strain, derived from displacement fields after a standard polar decomposition of the transformation gradient tensor. The independence of ε_{xx} from the Y coordinate (that is, the width direction) was confirmed by the experimental observations while the independence from the Z coordinate (that is, the depth direction) was legitimated by the small sample thickness. The two other stress components (shear: σ_{xy} and contraction: σ_{yy}) were computed by integrating the momentum equations [Wattrisse et al. 2001b]

$$\sigma_{xy}(X, Y, t) = -\frac{\partial \sigma_{xx}\big(x(X, Y, t), t\big)}{\partial x} y(X, Y, t),$$

$$\sigma_{yy}(X, Y, t) = \frac{\partial^2 \sigma_{xx}\big(x(X, Y, t), t\big)}{\partial x^2} \cdot \left(\frac{y(X, Y, t)^2}{2} - \frac{W_0^2(X) \exp(-\varepsilon_{xx}(X, t))}{8} \right).$$

The deformation energy locally developed by the material $w_{\text{def}}^{\bullet}(X, Y, t)$ was then estimated using Equation (2)

$$w_{\text{def}}^{\bullet} = \sigma_{xx} D_{xx} + 2\sigma_{xy} D_{xy} + \sigma_{yy} D_{yy}.$$

Thermal images. The infrared camera records the thermal radiations of the observed scene. Using the pixel calibration protocol described in [Honorat et al. 2005], we deduced the temperature variations of the specimen induced by the mechanical loading. To filter thermal data, local least-squares approximation of temperature fields was performed using the same set of polynomials as the one already used for visible images. In standard conditions, we estimated that the peak-to-peak thermal noise was about 200 mK (that is, before data filtering) and the range of the thermal noise dropped to 20 mK for standard filtering parameters. Moreover, the order of magnitude of the spatial resolution (in terms of pixel size) was about 0.4 mm and the temporal resolution was considered to be equal to the 0.04 s.

By integrating the heat Equation (4) over the depth of the sample [Chrysochoos and Louche 2000], and defining the mean thermal disequilibrium over the thickness between the sample and its surroundings by $\Theta = \overline{\theta - \theta^{\text{ref}}}$, we obtained the following 2D differential equation:

$$\rho C \dot{\Theta} - k\left(\frac{\partial^2 \Theta}{\partial x^2} + \frac{\partial^2 \Theta}{\partial y^2} \right) + \rho C \frac{\Theta}{\tau_{\text{th}}^{\text{2D}}} = w_{\text{h}}^{\bullet}. \tag{8}$$

The external heat supply r_{e} defined in Equation (4) is here taken into account by monitoring the uniform temperature variations $\theta^{\text{ref}} = T^{\text{ref}} - T_0^{\text{ref}}$ of an unloaded reference specimen of the same geometry placed near the specimen in the field of view of the IR camera

$$r_{\text{e}} = \rho C \dot{\theta}^{\text{ref}} + \frac{\theta^{\text{ref}}}{\tau_{\text{th}}^{\text{2D}}}.$$

The parameter $\tau_{\text{th}}^{\text{2D}}$ represents a time constant characterising heat losses by convection and radiation between the sample surfaces and the surroundings, and $\dot{\Theta} = \frac{\partial \Theta}{\partial t} + v \cdot \text{grad}\Theta$ is the particular time derivative of Θ, v representing the velocity vector.

Table 3 presents the different thermophysical parameters used in the heat source computations.

An overall estimate of the incertitude on heat sources should take into account every possible error sources associated with: (i) temperature accuracy, (ii) knowledge of the thermophysical parameters, (iii) relevance of the thermal modelling (heat exchanges, source distribution), and its identification, (iv)

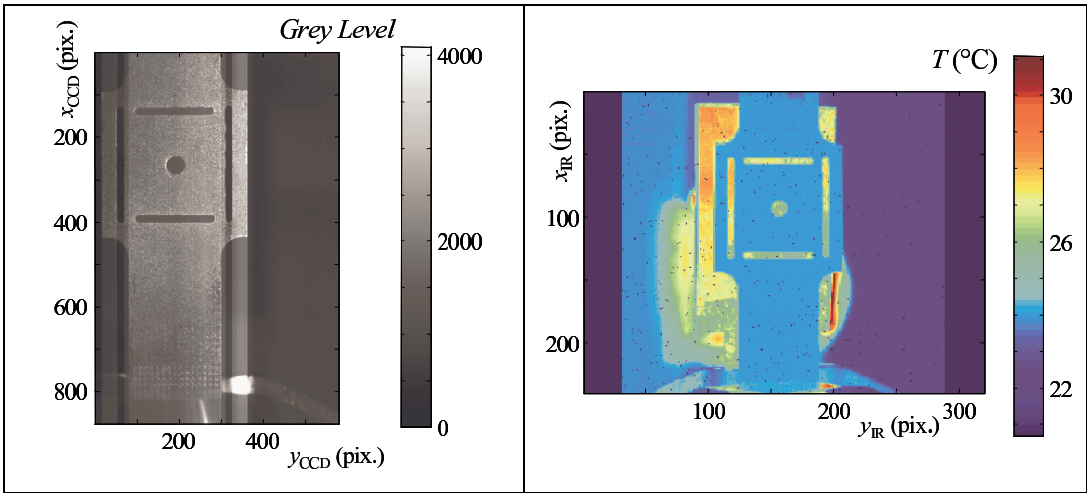

Figure 2. Calibration target: visible image (left); IR image (right).

mapping between kinematic and thermal data, (v) image processing robustness (derivation of discrete noisy temperature fields). Limiting the error analysis to items (i) and (v), we estimated the incertitude by computing the heat sources distribution from set of IR images of a nonloaded specimen. The parasitic sources derived from the image processing then gave an order of magnitude of the relative incertitude on the heat source fields. We found about a mean value of parasitic heat source of about 1.8×10^{-5} W mm^{-3} for a standard deviation of 2.7×10^{-5} W mm^{-3}.

In the case of localized flow, the time derivative should take the convective term $v \cdot \mathrm{grad}\,\Theta$ induced by the material flow into account. Once more, in accordance with the plane stress assumption, the smallness of the sample thickness and the high thermal diffusivity of the tested material, the depth-wise averaged temperatures were assumed to remain close to the surface temperatures. This enabled us to compute the convective term using the kinematic and thermal data.

Reference speckle and infrared images were mapped using a calibration target (see Figure 2). Comparing the visible and infrared images of the target, we determined the rigid body movements and the scale factor ratios between the two cameras.

For each acquisition time, the thermal data given by the IR camera (measured in the current, deformed configuration) were linearly interpolated spatiotemporally using the positions of the deformed configuration given by the DIC computation. This operation allowed us to track material particles associated with the DIC mesh, and it thus enabled us to compute temperature variations in the Lagrangian configuration. Figure 3 illustrates the distribution of temperature variations after 50 s of loading. Figure 3 (left) gives

ρ (kg m^{-3})	C (J kg^{-1} K^{-1})	k (W m^{-1} K^{-1})	$\lambda\, 10^6$(K^{-1})	T_0^{ref} (K)	$\tau_{\mathrm{th}}^{\mathrm{2D}}$ (s)
7800	480	60	12.5	293	32

Table 3. Thermophysical parameters.

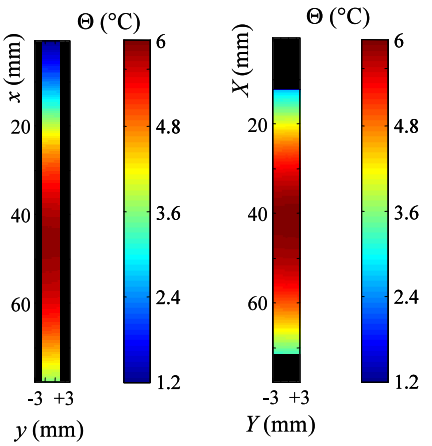

Figure 3. Thermal images represented in the current configuration (O, x, y) (left) and in the reference configuration (O, X, Y) (right).

the temperature distribution in the current (Eulerian) configuration, while Figure 3 (right) shows the temperature distribution brought back in the reference (Lagrangian) configuration. Both figures are associated with a material zone, initially of 6 mm width, centred on the gauge part of the specimen.

To illustrate the temperature patterns throughout the test, we plotted, in a single diagram, the time course of the temperature longitudinal profile captured in the middle of the sample width ($y = Y = 0$ mm). Figure 4 represents variations in the profile throughout the test, in the Eulerian configuration ($\theta(x, y = 0, t)$, Figure 4, left) and in the Lagrangian configuration ($\theta(X, Y = 0, t)$, Figure 4, right). In these figures, the horizontal axis represents the time while the vertical axis represents the sample longitudinal axis in the current configuration (x in Figure 4 (left)) or in the initial configuration (X in Figure 4 (right)). A conventional stress versus time curve was also superimposed in order to link the local thermal data to the overall mechanical loading. The paths of three MSE (named $\boldsymbol{A}$, $\boldsymbol{B}$ and $\boldsymbol{C}$) were plotted to illustrate the material flows. Element $\boldsymbol{A}$ is quite specific as it is the fracture point. Naturally, as material particles remain fixed in the Lagrangian configuration, their paths are simple horizontal lines in Figure 4 (right).

We can observe that the level curves in Figure 4 (left) appear to be noisier than those of Figure 4 (right). This is simply due to the fact that the Eulerian representation was here constructed without any temperature filtering (crude data) unlike the Lagrangian one.

The temperature time and spatial partial derivatives were then computed using a local polynomial fitting technique [Moreau et al. 2004]. Naturally, the spatial derivation was performed with respect to the current deformed state. In the Lagrangian configuration, the particular derivative of the temperature is equal to the partial time derivative $\dot{\Theta} = \partial\Theta/\partial t(X, Y = 0, t)$ and can thus be easily computed. Figure 5 (top left) gives the particular time derivative of the temperature during the test, while Figure 5 (top right) shows changes in the convective term $v\ (x, y = 0, t) \cdot \mathrm{grad}\ \Theta\ (x, y = 0, t)$. This latter term can here reach up to 50% of the particular derivative and thus cannot be neglected in the time derivation. To more easily understand the particular distribution of the convective terms during strain localization, the longitudinal

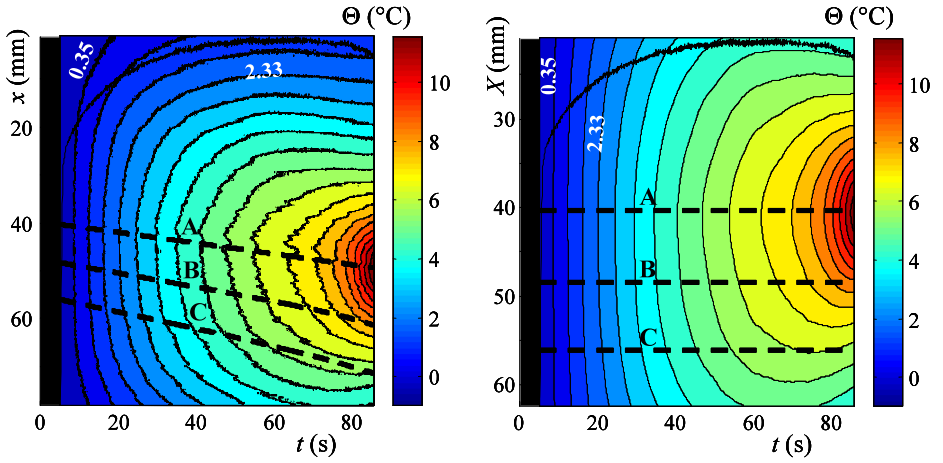

Figure 4. Temperature profile variations during a tensile test performed on a IF–Ti steel represented ($\delta\theta$ between two consecutive level curves: 0.66 K). The deformed configuration (O, x, t) (left); and the reference configuration (O, X, t) (right).

thermal gradients $\partial\Theta/\partial x(X, Y = 0, t = 80)$ and the longitudinal velocity profile $v_x(X, Y = 0, t = 80)$ were plotted in Figure 5 (bottom) as functions of the Lagrangian coordinate X. The strain localization zone is characterized by a high strain rate in the necking region and inversion of the thermal gradient induced by the combined effect of the concentration of heat sources and heat diffusion.

Data processing validation

DIC and IRT image processing algorithms have been widely presented and checked in previous works [Wattrisse et al. 2001a; Chrysochoos and Louche 2000]. In what follows, we tested the reliability of the energy balance construction by comparing the overall heat sources $w_{\mathrm{h}}^{\bullet}$ with the mechanical energy rate $w_{\mathrm{def}}^{\bullet}$ developed by the material. Indeed, as the elastic deformation energy and the heat induced by thermoelastic coupling remain small in plasticity, the plastic work and dissipated energy must be of the same order of magnitude.

Hereafter, the validation mainly deals with the local deformation energy. As it is experimentally impossible to impose a heterogeneous distribution of mechanical energy on a structure, we chose to check the image processing through numerical tests. A displacement-controlled tensile test was simulated using a finite element code (Cast3M) and a Prager elastoplastic model with linear kinematic hardening. We performed a three-dimensional computation in order to account for the triaxiality effect in the development of the neck. Furthermore, to obtain localized stress and strain patterns consistent with the development of necking, we used an initial geometry corresponding to an already necked specimen. To facilitate the three-dimensional FE computation (no need of remeshing due to mesh distortion), we chose to simulate the straining on a thicker specimen of about 2 mm (to be compared with the 0.3 mm of the real specimens). We were thus able to reproduce localized flow using a simple and thus easily identifiable homogeneous model. Figure 6 shows the initial geometry of the specimen used in the computation, measured by a

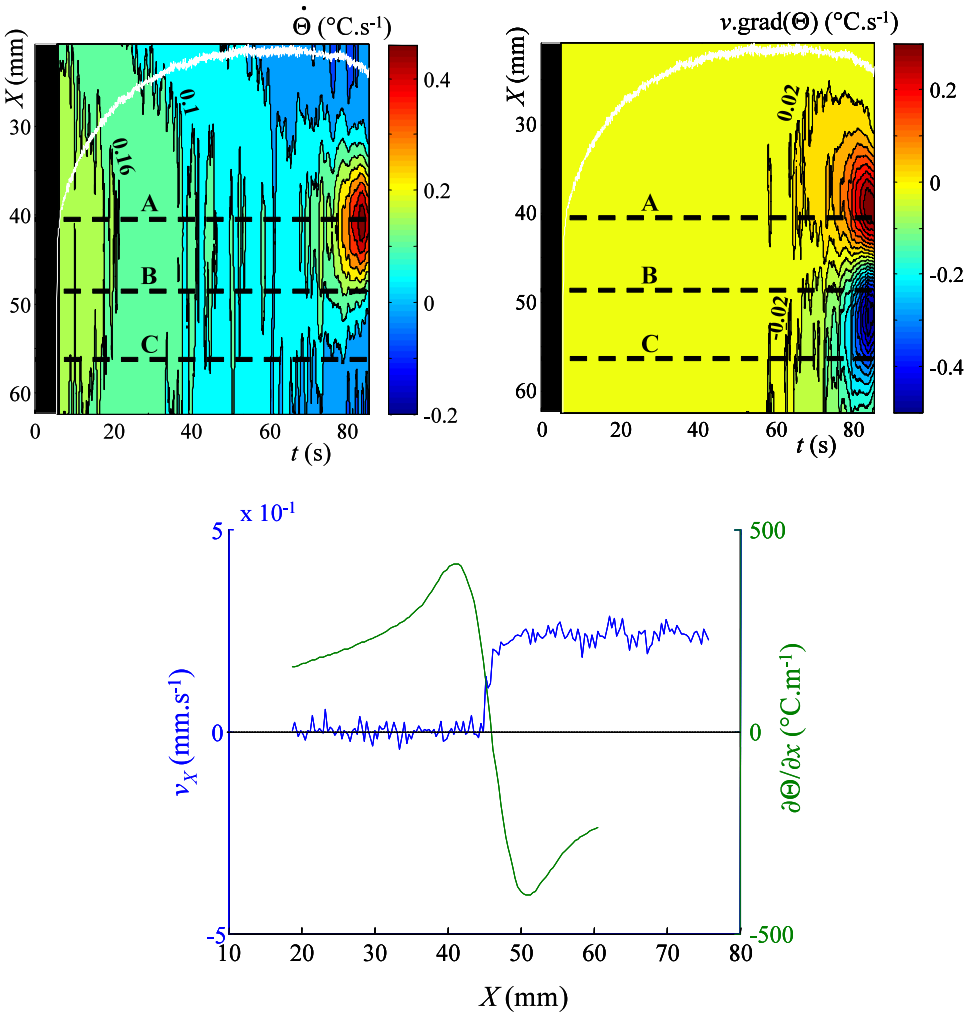

Figure 5. Time derivation of the temperature field: particular derivative ($0.06\,\mathrm{K\,s^{-1}}$) between two level curves (top left); convective term ($0.04\,\mathrm{K\,s^{-1}}$) between two level curves (top right); and Ox profiles of the longitudinal thermal gradient and velocity at $t = 80\,\mathrm{s}$ (bottom).

3-axis measurement machine. It clearly highlights the presence of the neck in the middle of the sample $(X, Y) = (0, 0)$.

The material properties used in the FE computation are given in Table 4. The upper side of the sample was fixed and a vertical displacement was imposed on its lower side. We deduced the mechanical energy rate distribution $w^{\bullet}_{\mathrm{def}}(X, Y, Z, t)$ from the stress and strain-rate patterns given by the computation. By averaging this quantity over the specimen depth, we obtained the time patterns of the 2D distribution of the mechanical energy rate $w^{\bullet}_{\mathrm{def}}(X, Y, t) = 1/D_0 \int_{-D_0/2}^{D_0/2} w^{\bullet}_{\mathrm{def}}(X, Y, Z, t)\,dZ$. We also extracted the in-plane components of the displacement vector of points located on the sample surface to analyze.

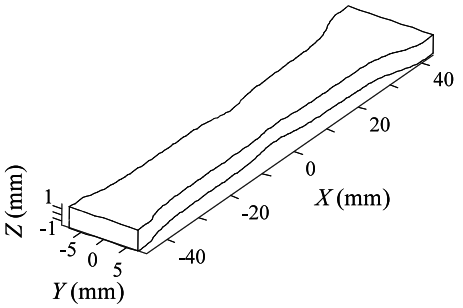

Figure 6. Initial geometry of the specimen used in the finite element computation.

The numerical displacement fields represented the kinematic data obtained by DIC. They were used to compute the in-plane strain-rate $D(X, Y, t)$ and the stress tensors $\sigma(X, Y, t)$ with the data processing described in the previous section.

In Figure 7, we compared the distribution of $w^{\bullet}_{\text{def}}$ given by the finite element simulations with those associated with the depthwise-averaged tensor product $\sigma : D$. Figure 8 shows the longitudinal profile of the $w^{\bullet}_{\text{def}}$ and $\sigma : D$ integrated over slides of equivalent length ($\Delta X = 0.827\,\text{mm}$) $D_0 \times W_0(X) \times \Delta X$ of the specimen. As expected, the mechanical energy was localized in the neck. Even in this highly heterogeneous triaxial situation, we obtained a satisfactory correlation on the distribution, and quantitatively good estimates of the mechanical energy rate amplitudes.

Experimental results

DIC analysis reveals variations in various kinematical data such as the Eulerian strain-rate tensor D, and the acceleration vector γ. Figure 9 (left) shows the spatiotemporal diagram of the strain-rate component $D_{xx}(X, Y = 0, t)$, and Figure 9 (right) illustrates variations in the axial components of the acceleration vector $\gamma_X(X, Y = 0, t)$. All the results presented here correspond to the same displacement-controlled test, with a conventional strain-rate $\dot{\varepsilon}_c$ of about of $5 \times 10^{-3}\,\text{s}^{-1}$, performed on IF–Ti steel.

At the beginning of the test, D_{xx} was lower than $\dot{\varepsilon}_c$ throughout the test section of the specimen because of the finite elastic stiffness of the testing machine frame. The early and steady narrowing of the level curves indicates that the necking region (located around point A) gradually concentrates before the maximum load is reached. This also means that the gauge part of the sample is no longer uniformly strained (and stressed), thus complicating extraction of the material response and consequently its modelling and identification.

Figure 9 (right) shows that the acceleration amplitude is negligible compared with the gravity acceleration, which is classically ignored in the case of quasistatic tensile tests. This experimental result and the

Young modulus E (MPa)	Poisson ratio ν	Yield stress σ_0 (MPa)	Hardening modulus H (MPa)
210000	0.3	315	5200

Table 4. Material properties used for the finite element computation.

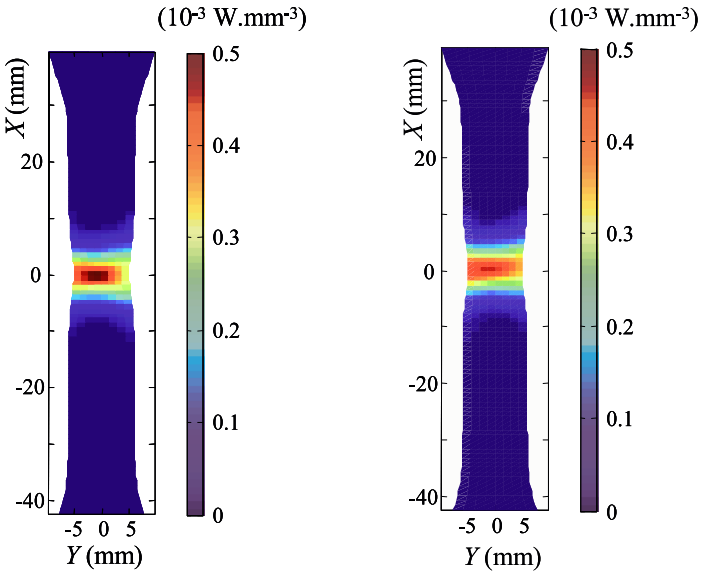

Figure 7. Distribution of the deformation energy rate given by the finite element code (left) and computed as $\sigma : D$ (right).

sample geometry (thin specimen) confirms the hypotheses used in the stress calculation (see section on *Data processing*). At the beginning of the test, uniform acceleration profiles of "significant" level (that is, $10^{-5}\,\mathrm{m\,s^{-2}}$) can be observed. They are induced by a combination of the mechanical gaps and finite stiffness of the testing machine and the time fitting of displacement data. As it was already shown in a

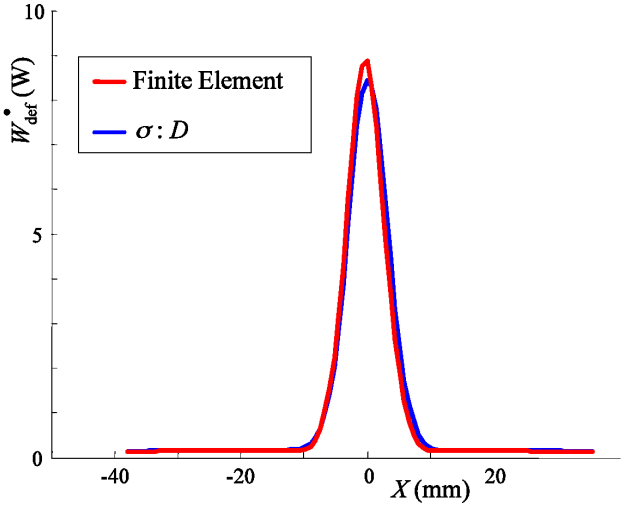

Figure 8. Longitudinal profiles of the deformation energy rate received by equally-spaced, 0.827 mm width, slices of the sample derived from kinematical data with the equilibrium equations (computed as $\sigma : D$) and directly computed within the FE code.

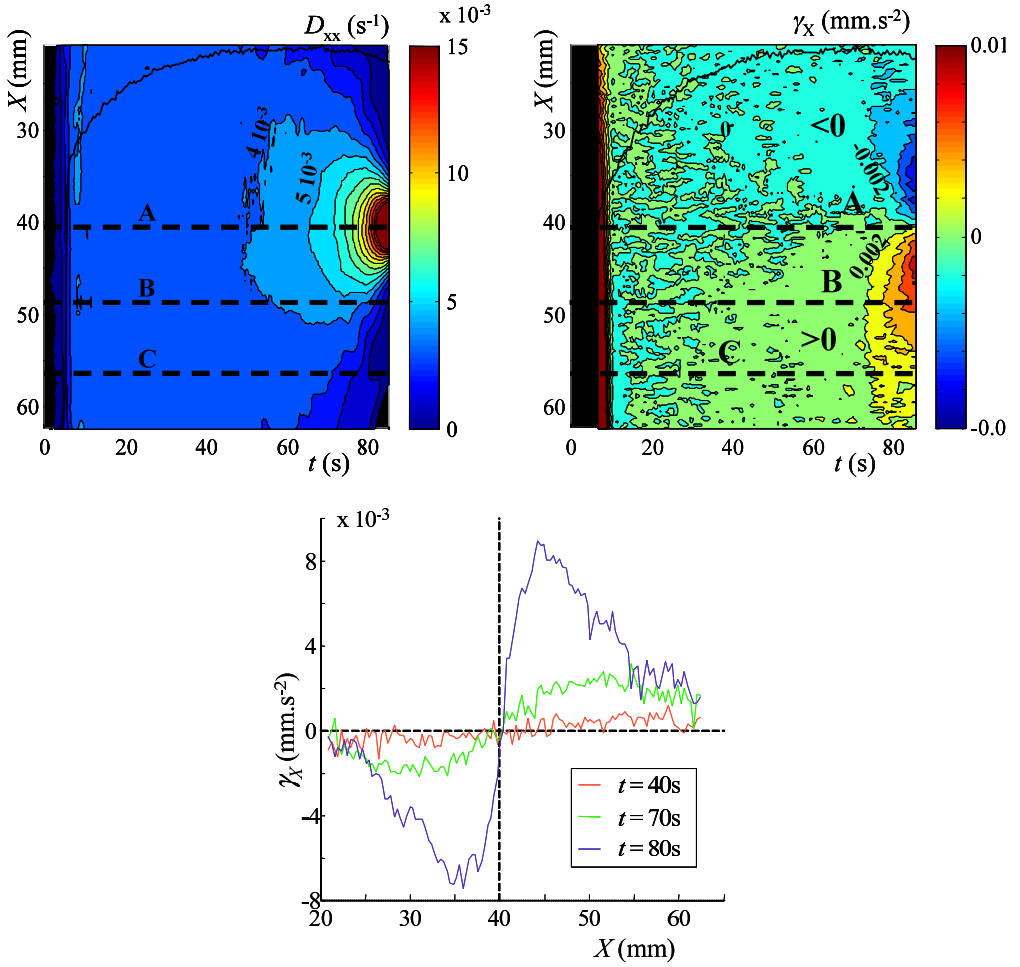

Figure 9. Spatiotemporal variation in $D_{xx}(X, 0, t)$, $10^{-3}\,\mathrm{s}^{-1}$ between two level curves (left) and $\gamma_X(X, 0, t)$, $0.002\,\mathrm{mm\,s}^{-2}$ between two level curves (right). Different profiles of gx acceleration at $t = 40$, 70, 80 s are also shown (bottom).

previous paper [Wattrisse et al. 2001b], a steady concentration of level curves of positive and negative acceleration, distributed on both sides of the necking zones, can be clearly observed. The section where the fracture will take place (that is, MSE ***A***) is then characterized by zero acceleration. This cross-section can be easily predetermined on the basis of Figure 9 (bottom) where acceleration profiles captured at time $t = 40$ s, 70 s, and 80 s intersect in a given cross-section. It seems like the specimen knew where the crack would take place a long time before the crack occurred. Moreover, the odd distribution of acceleration profiles with respect to MSE ***A*** is consistent with a symmetric strain distribution centred on the neck.

The heterogeneity of the specimen response can also be clearly observed in Figure 10, illustrating variations in the longitudinal distribution of tensile stress throughout the test.

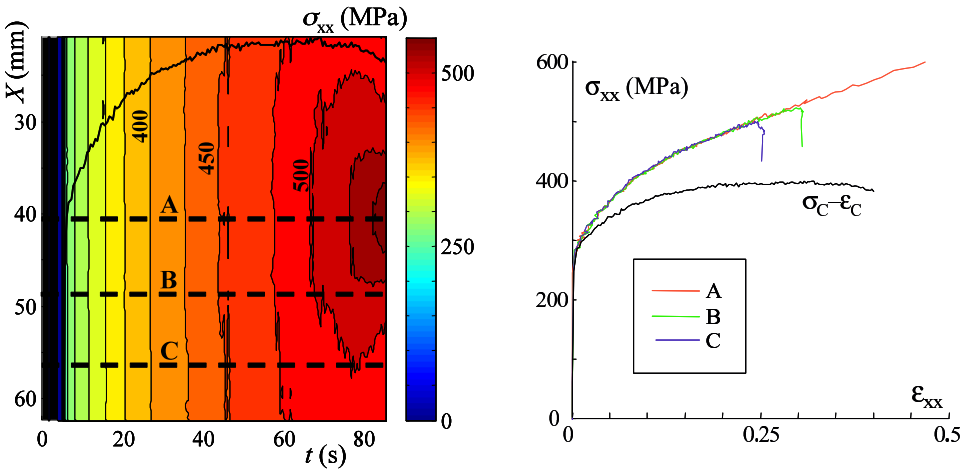

Figure 10. Mechanical response. Time duration of $\sigma_{xx}(X, 0, t)$, 25 MPa between two level curves (left); stress-strain diagrams of the three MSE ***A***, ***B*** and ***C*** with the conventional stress-strain response of the specimen (right).

As expected, the stress was rather homogeneous in the sample gauge part at the beginning of the test. A stress concentration appeared in the necking zone as localization developed. Combining the local stress and strain measurements, we plotted the local stress-strain correspondence in the MSE, denoted ***A***, ***B*** and ***C*** (Figure 10, right). All the curves describe a unique path at the beginning of hardening. Nevertheless, as the imposed macroscopic strain ε_C increased, the stress amplitudes at ***A***, ***B*** and ***C*** rapidly diverged. Once the structure started to soften, σ_{xx} decreased in sections in which the strain-rate vanished (***B*** and ***C***), while it continued to increase in the section of the current necking zone. It thus seems that softening of the sample, translated by a nonmonotone load-elongation curve, was induced by heterogeneous hardening accompanied by elastic unloading in cross-sections outside the localization zone.

Figure 11 (left) presents the spatiotemporal distribution of the deformation energy rate during strain hardening. The data processing was stopped before the rapid growth of localized necking in order to consider relatively low temperature, stress and strain-rate gradients. In the late stages of localization, the spatial resolution of the method was not sufficient to catch the high thermal and high kinematical gradients. Investigations require then to change the scale of observation or the data processing parameters. The gradual narrowing of level curves observed in Figure 11 (left) again highlights the progressive development of localization, but now in terms of deformation energy.

The different terms on the left-hand side of Equation (8) were successively calculated to estimate the overall heat source. Figure 11 (right) shows heat source variations along the longitudinal axis of the sample. Again, the contour plot revealed progressive narrowing of the level curves. We obviously attributed the concentration of heat sources to the development of dissipative mechanisms due to localization of hardening and damage.

The intrinsic dissipation was deduced from Equation (8). For simplicity, we assumed a linear, isotropic thermoelastic behavior. The quantity $w^{\bullet}_{\text{tec}}$ was determined using the computed stress data and following

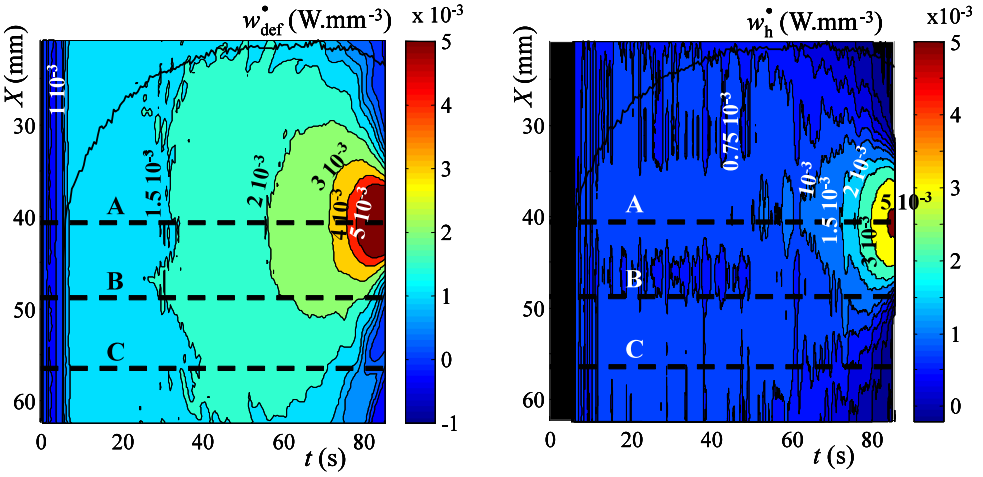

Figure 11. Spatiotemporal variations in energy rates: $w^{\bullet}_{\mathrm{def}}(X,0,t)$ (left); $w^{\bullet}_{\mathrm{h}}(X,0,t)$ (right).

the approximated definition

$$w^{\bullet}_{\mathrm{tec}} \approx -\lambda T_0 \mathrm{tr}(\dot{\sigma}), \tag{9}$$

where λ stands for the linear thermal dilatation coefficient. The validity of this approximation is mainly due to the smallness of λ. In previous papers we already underlined that Equation (9) holds true as long as

$$\frac{9K\lambda^2}{\rho C} T \approx \frac{9K\lambda^2}{\rho C} T_0 \ll 1,$$

where K is the bulk elastic modulus.

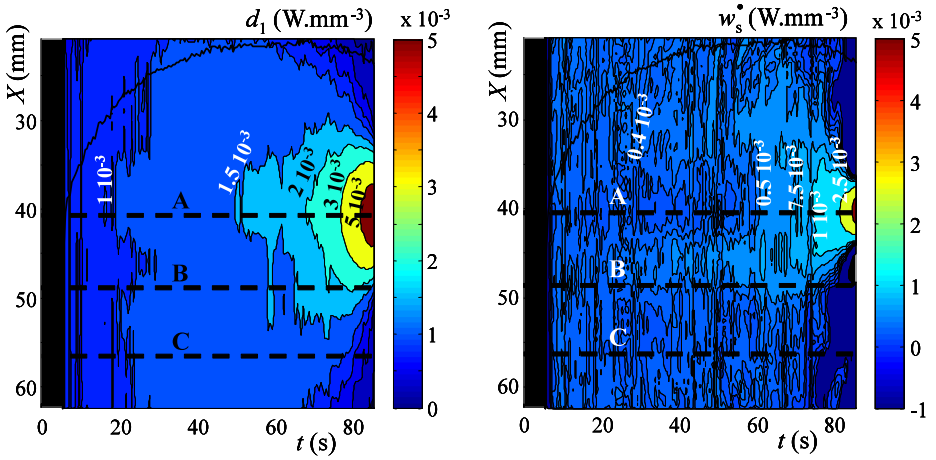

Figure 12. Spatiotemporal variations in $d_1(X,0,t)$ (left); $w^{\bullet}_{\mathrm{s}}(X,0,t)$ (right).

During elastic loading and in the early stages of plasticity, the intrinsic dissipation was very small (see Figure 12, left), and then increased with hardening. The same trends could be observed in the d_1 and $w_h^\bullet$ patterns.

According to Equations (1)–(3), the stored energy rate was then estimated by the relation

$$w_s^\bullet = w_{def}^\bullet - d_1 - w_e^\bullet.$$

The local evaluation of stored energy rate obtained via Equation (6) must be considered with caution owing to the successive approximations. Nevertheless, we decided to show a detailed picture of the stored energy rate in Figure 12 (right). The distribution appears to be heterogeneous and concentrated in the vicinity of the necking region.

The energy distributions ($w_{def}(X, Y, t)$, $w_d(X, Y, t)$, $w_s(X, Y, t)$, ...) were computed by integrating the corresponding energy rates over time. Figure 13 (left) shows variations in the different energies involved in the energy balance at MSE ***A***, ***B*** and ***C*** for the same macroscopic applied load. These energies are plotted with respect to the local strain reached at each point. The test heterogeneity is noted by the fact that the curves corresponding to the three points are not identical: the trends are fairly similar, but the energy levels reached are not the same (they increase as they get close to the localization zone). Note that we did not observe significant decrease of the stored energy for large strain, particularly in the necking zone. We have to mention that this last result then differs from findings recently published by Oliferuk and Maj [2007] who observed strong decreases of the (overall) stored energy at the maximum load defining the famous Considère instability point. It is worth noting that the method developed to estimate the dissipated energy used an electrical analogy, these authors tuning in Joule's effects to determine the dissipated heat, the adjustment of the electrical power being controlled by the thermal response.

Figure 13 (right) shows variations in the Taylor–Quinney stored energy ratio F_w with the local strain reached at MSE ***A***, ***B*** and ***C***. We observed negative values of the stored energy at the beginning of strain hardening induced by an underestimate of the thermoelastic source intensity. This poor estimate was associated with disputable values of standard thermoelastic constants extracted from the literature.

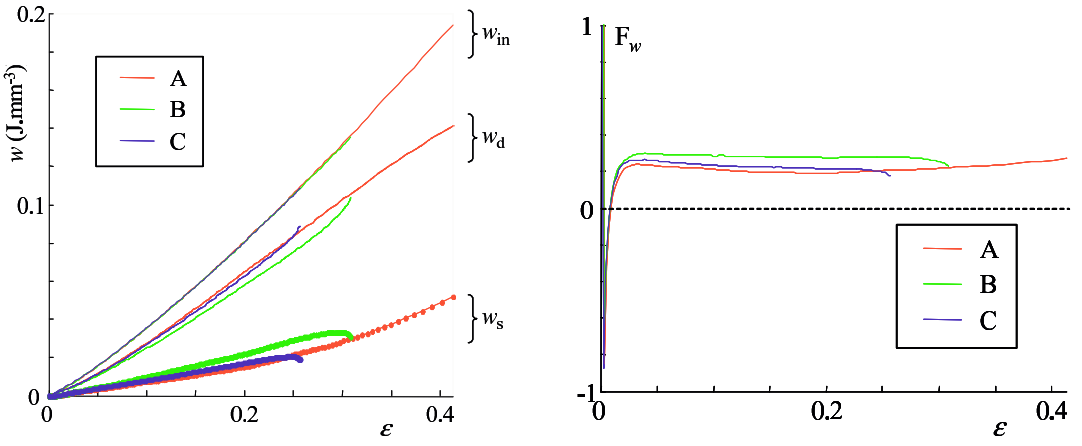

Figure 13. Energy balance at MSE ***A***, ***B*** and ***C***: variations in the stored w_s, dissipated w_d and inelastic w_{in} energies (left); local Taylor–Quinney ratio F_w (right).

This effect on the stored energy ratio is here naturally amplified by the computation of a ratio involving two small noisy amounts of energy. Once the anelastic energy becomes significant, the F_w variations are fairly similar from one point to another: rapid increase during the first stages of hardening, until a maximum is reached ($F_w \approx 0.25$), followed by a small decrease ($F_w \approx 0.2$). Further tests on different steel grades are under way to confirm these trends. Contrary to most literature results, in this study the Taylor–Quinney coefficient distributions were determined on relatively small volume elements (typically around $1\,\mathrm{mm}^3$). The main advantage is to reduce the effects of localization on the energy balance. In return, the signal–to–noise-ratios are lower, so well controlled data processing techniques are required.

Conclusions

In conclusion, we designed a set-up that combined DIC with IRT. Many technical difficulties were overcome and the first results presented in this paper are encouraging. Both imaging techniques gave similar spatial distributions and temporal patterns concerning heat sources and mechanical energy rates throughout the test (especially during strain localization). The capabilities of the imaging techniques allowed us to check the local quasistatic character of strain localization. Despite the low acceleration intensities, the kinematical image processing showed that the cross-section where the crack initiated was early characterized during hardening by zero acceleration, dividing the gauge part of the sample into two parts where the accelerations were positive and negative, respectively. The combination of thermal and kinematical data illustrated that heat involved by matter convection could represent up to more than 50% of the overall heat sources. This underlined the necessity of combining DIC with IRT as soon as localization occurs.

However, several metrology problems remain. The next stage is to increase the signal-to-noise ratios of both cameras to obtain more reliable quantitative results. Moreover, the data processing will be improved in order to better account for the last localization stages. The fine knowledge of the material parameters involved in the heat conduction equation, and their possible variations with the material state, are critical for the heat source computation. Collaborations are under way with several research teams, within the framework of the French National Research Agency program, to better characterize the influence of hardening and damage on the thermophysical properties of materials.

Local determination of dissipated and stored energies is essential to test the reliability of the constitutive equations proposed in thermomechanical formalism of plasticity and damage. This could give rise to a method for separating hardening from damage, inasmuch as the latter is purely dissipative, unlike the first one. This should be performed on elastoplastic cohesive zone models used to numerically manage fracture in heterogeneous materials.

References

[Batra and Chen 2001] R. C. Batra and L. Chen, "Effect of viscoplastic relations on the instability strain, shear band initiation strain, the strain corresponding to the minimum shear band spacing, and the band width in a thermoviscoplastic material", *Int. J. Plasticity* **17**:11 (2001), 1465–1489.

[Béranger et al. 1994] G. Béranger, G. Henry, and G. Sanz, *Le livre de l'acier*, Lavoisier, Paris, 1994.

[Campagne et al. 2005] L. Campagne, L. Daridon, and S. Ahzi, "A physically based model for dynamic failure in ductile metals", *Mech. Mat.* **37**:8 (2005), 869–886.

[Chrysochoos and Louche 2000] A. Chrysochoos and H. Louche, "An infrared image processing to analyse the calorific effects accompanying strain localisation", *Int. J. Eng. Sci.* **38**:16 (2000), 1759–1788.

[Chrysochoos and Martin 1989] A. Chrysochoos and G. Martin, "Tensile test microcalorimetry for thermomechanical behaviour law analysis", *Mat. Sci. Eng. A* **108** (1989), 25–32.

[Chu et al. 1985] T. C. Chu, W. F. Ranson, and M. A. Sutton, "Applications of digital-image-correlation techniques to experimental mechanics", *Exp. Mech.* **25**:3 (1985), 232–244.

[Guduru et al. 2001] P. R. Guduru, A. T. Zehnder, A. J. Rosakis, and G. Ravichandran, "Dynamic full field measurements of crack tip temperatures", *Eng. Fract. Mech.* **68**:14 (2001), 1535–1556.

[Halphen and Nguyen 1975] B. Halphen and Q. S. Nguyen, "Sur les matériaux standards généralisés", *J. de Méc.* **14**:1 (1975), 39–63.

[Honorat et al. 2005] V. Honorat, S. Moreau, J.-M. Muracciole, A. Chrysochoos, and B. Wattrisse, "Calorimetric analysis of polymer behaviour using a pixel calibration of an I. R. F. P. A. camera", *Int. J. Q. I. R. T.* **2**:2 (2005), 153–172.

[Lemaitre and Chaboche 1985] J. Lemaitre and J.-L. Chaboche, *Mécanique des matériaux solides*, Dunod, Paris, 1985.

[Lubliner 1991] J. Lubliner, "A simple model of generalized plasticity", *Int. J. Solids Struct.* **28**:6 (1991), 769–778.

[Mercier and Molinari 1998] S. Mercier and A. Molinari, "Steady-state shear band propagation under dynamic conditions", *J. Mech. Phys. Solids* **46**:8 (1998), 1463–1495.

[Moreau et al. 2004] S. Moreau, J.-M. Muracciole, and B. Wattrisse, "Experimental energy balance for thermoplastics stretched at room temperature", in *Proceedings of the 12th I. C. E. M. Conference* (Bari, Italy), vol. CDROM 8, 2004.

[Oliferuk and Maj 2007] W. Oliferuk and M. Maj, "Plastic instability criterion based on energy conversion", *Mat. Sci. Eng. A* **462**:1-2 (2007), 363–366.

[Rittel 1999] D. Rittel, "On the conversion of plastic work to heat during high strain rate deformation of glassy polymers", *Mech. Mat.* **31**:2 (1999), 131–139.

[Rosakis et al. 2000] P. Rosakis, A. J. Rosakis, G. Ravichandran, and J. Hodowany, "A thermodynamic internal variable model for the partition of plastic work into heat and stored energy in metals", *J. Mech. Phys. Solids* **48**:3 (2000), 581–607.

[Rusinek et al. 2007] A. Rusinek, R. Zaera, and J. Klepaczko, "Constitutive relations in 3-D for a wide range of strain rates and temperatures: application to mild steels", *Int. J. Solids Struct.* **44**:17 (2007), 5611–5634.

[Schmidt et al. 1945] A. O. Schmidt, O. W. Gilbert, and A. Boston, "Thermal balance method and mechanical investigation for evaluating machinability", *Trans. A.S.M.E.* **67** (1945), 225–232.

[Shenogin et al. 2002] S. V. Shenogin, G. W. Hohne, and E. F. Oleinik, "Thermodynamics of the pre-yield deformation behavior of glassy polymers: measurements with new deformation calorimeter", *Thermochim. Acta* **391**:1-2 (2002), 13–23.

[Taylor and Quinney 1934] G. I. Taylor and H. Quinney, "The latent energy remaining in a metal after cold working", *P. Roy. Soc. Lond. A Mat.* **143**:849 (1934), 307–326.

[Wattrisse et al. 2001a] B. Wattrisse, A. Chrysochoos, J.-M. Muracciole, and M. Némoz-Gaillard, "Analysis of strain localization during tensile tests by digital image correlation", *Exp. Mech.* **41**:1 (2001), 29–39.

[Wattrisse et al. 2001b] B. Wattrisse, A. Chrysochoos, J.-M. Muracciole, and M. Némoz-Gaillard, "Kinematic manifestations of localisation phenomena in steels by digital image correlation", *Eur. J. Mech. A Solids* **20**:2 (2001), 189–211.

[Zehnder et al. 1998] A. T. Zehnder, E. Babinsky, and T. Palmer, "Hybrid method for determining the fraction of plastic work converted to heat", *Exp. Mech.* **38**:4 (1998), 295–302.

Received 18 Dec 2007. Revised 9 Jun 2008. Accepted 19 Jun 2008.

ANDRÉ CHRYSOCHOOS: chryso@lmgc.univ-montp2.fr
LMGC UM 5508 CNRS UMII, CC 081, Université Montpellier II, Place E. Bataillon, 34095 Montpellier Cedex, France

BERTRAND WATTRISSE: wattrisse@lmgc.univ-montp2.fr
LMGC UM 5508 CNRS UMII, CC 081, Université Montpellier II, Place E. Bataillon, 34095 Montpellier Cedex, France

JEAN-MICHEL MURACCIOLE: muracciole@lmgc.univ-montp2.fr
LMGC UM 5508 CNRS UMII, CC 081, Université Montpellier II, Place E. Bataillon, 34095 Montpellier Cedex, France

YVES EL KAÏM: elkaim@lmgc.univ-montp2.fr
LMGC UM 5508 CNRS UMII, CC 081, Université Montpellier II, Place E. Bataillon, 34095 Montpellier Cedex, France